Journal of Materials Chemistry A

ROYAL SOCIETY OF CHEMISTRY

PAPER

View Article Online
View Journal

Cite this: DOI: 10.1039/d6ta01278g

A multifunctional bismuth-based metal–organic framework with record-high porosity, rare topology, and efficient visible light photocatalysis

Michelle Åhlén, †[a] Ha Phan, †[a] Mariusz Kubus,[b] James N. McPherson, [b] Francoise M. Amombo Noa,[c] Lars Öhrström, [c] Kasper S. Pedersen, [b] Maria Strømme [a] and Ocean Cheung *[a]

Here, we report the bismuth-based metal–organic framework (MOF), UU-206, constructed from $Bi(NO_3)_3 \cdot 5H_2O$ and an extended tetraphenylenethylene-cored octacarboxylate linker (H_8ettb). UU-206 crystallizes as a three-dimensional framework that can be described by the rare **msg**/**wxs** nets and features four one-dimensional channels with pore diameters of approximately 6–11 Å. Nitrogen sorption isotherms at −196 °C reveal a Brunauer–Emmett–Teller (BET) surface area of 1119 $m^2\ g^{-1}$ and a total pore volume of 0.55 $cm^3\ g^{-1}$, placing UU-206 among the most porous Bi-MOFs reported to-date. Optical and electrochemical measurements show that the material is a visible light responsive semiconductor ($E_g \approx 2.68$ eV) with efficient photoinduced charge separation. Consequently, UU-206 functions as an efficient heterogeneous photocatalyst for the aerobic oxidative condensation of amines to imines, delivering up to 86% yield under visible light irradiation and outperforming related Bi-based materials. Notably, the reaction can also be driven by low-intensity natural sunlight at high latitudes, underscoring the potential of UU-206 as a platform for solar-driven organic transformations. Furthermore, this work demonstrates how integrating polytopic chromophore linkers with Bi-cluster nodes provides a powerful design strategy for developing multifunctional MOFs with high porosity, rare topology, and efficient visible light photocatalysis.

Received 10th February 2026
Accepted 13th April 2026

DOI: 10.1039/d6ta01278g

rsc.li/materials-a

1. Introduction

Metal–organic frameworks (MOFs) are renowned for their high porosity and modular pore structure,[1,2] which have enabled their utilization in applications ranging from gas storage and separation to energy storage and catalysis.[3,4] In particular, bismuth-based MOFs (Bi-MOFs)[5–11] are an emerging group of framework materials that are promising visible-light photocatalysts due in part to the semiconducting properties of certain inorganic bismuth clusters.[12] By interlinking these clusters with organic ligands, further modulation of the catalytic properties can be achieved that can significantly enhance the charge–transfer properties of the materials.[13] For instance, efficient degradation of the organic dye Rhodamine B under visible-light irradiation was achieved by the 2-mercaptonicotinic acid-linked Bi-MOF Bi-mna.[14] More than 95% of the dye was removed in the presence of the MOF, compared with less than 10% for commercial α-Bi_2O_3. This enhanced performance was attributed to ligand-to-ligand charge transfer (LLCT) processes within Bi-mna, and this material served as one of the earliest examples of a visible light-active Bi-MOF photocatalyst. Utilizing electron-rich polytopic chromophore linkers, such as pyrene- or tetraphenylenethylene-cored carboxylate compounds, can furthermore not only enhance the charge-transfer[15,16] and the light-harvesting[17–19] properties of MOFs, but also give rise to diverse framework topologies that influence the pore structure of MOFs. In particular, the unpredictable coordination environment of Bi^{3+} ions often gives rise to topological complex structures, owing to their large ionic radius and high coordination number,[20] as observed in inorganic compounds such as Bi_2PdO_4.[21] Additionally, polynuclear secondary building units exhibiting diverse motifs have been observed in Bi-MOFs such as CAU-17, constructed from trimesic acid, in which 54 unique nodes were identified along with 135 edges forming a complex net rarely seen in MOF structures.[5] The limited number of existing Bi-MOFs makes the search for novel Bi-MOFs highly interesting from a scientific viewpoint, and also opens up possibilities for adopting Bi-MOFs in various applications. Here, we showcase a novel Bi-MOF, UU-206, which has an unusual topology and one of the highest porosities reported

[a]Department of Materials Science and Engineering, Ångström Laboratory, Uppsala University, Uppsala SE-751 03, Sweden. E-mail: ocean.cheung@angstrom.uu.se
[b]Department of Chemistry, Technical University of Denmark, Kongens Lyngby DK-2800, Denmark
[c]Department of Chemistry and Chemical Engineering, Chalmers University of Technology, SE-412 96, Gothenburg, Sweden
† Both authors contributed equally.

among all Bi-MOFs to-date. The efficient photocatalytic property of UU-206 and its performance in catalyzing the condensation of amines to imines at ambient conditions are demonstrated under both high and low intensity visible light.

2. Experimental

2.1. Materials

Bismuth(III) nitrate pentahydrate ($Bi(NO_3)_3 \cdot 5H_2O$) 98% was purchased from Sigma-Aldrich, 4′,4‴,4⁗,4⁗′′-(ethene-1,1,2,2-tetrayl)tetrakis(([1,1′-biphenyl]-3,5-dicarboxylic acid)) (H_8ettb) >97% from Tensus Biotech. Benzylamine (**1a**), 4-*tert*-butylbenzylamine (**1b**), 4-methoxybenzylamine (**1c**), 3-methoxybenzylamine (**1d**), 2-methoxybenzylamine (**1e**), 4-fluorobenzylamine (**1f**), 4-chlorobenzylamine (**1g**), 4-bromobenzylamine (**1h**), 3-bromobenzylamine (**1i**), 2-bromobenzylamine (**1j**), 4-(trifluoromethyl)benzylamine (**1k**), 2-thiophenemethylamine (**1l**), and ammonium chloride (NH_4Cl) ≥99% were purchased from Fisher Chemicals. Anhydrous sodium sulfate (Na_2SO_4) 99% was purchased from Thermo Scientific. Anhydrous *N*,*N*-dimethylformamide (DMF) 99.8%, acetonitrile (MeCN) 99.5%, ethyl acetate (EtOAc) 99.5%, *n*-hexane ≥95%, dichloromethane (CH_2Cl_2) 99.8%, formic acid (HCOOH) 99–100%, triethyl amine (Et_3N) ≥99%, deuterated chloroform ($CDCl_3$) 99.8%, deuterated methanol (CD_3OD) ≥99.9% were purchased from VWR Sweden. Absolute ethanol (EtOH) 99.9% was purchased from Solveco. All reagents were used as received without further purification, except for anhydrous MeCN, which was obtained by treating commercially available MeCN over activated 4 Å molecular sieves.

2.2. Synthesis of UU-206

$Bi(NO_3)_3 \cdot 5H_2O$ (19.3 mg, 0.040 mmol, 1.1 equiv.) and HCOOH (100 μL, 2.65 mmol, 72 equiv.) were added to a vial containing anhydrous DMF (5.0 mL). The mixture was sonicated for 5 min until $Bi(NO_3)_3 \cdot 5H_2O$ was fully dissolved, yielding mixture A. In another vial, H_8ettb (36.35 mg, 0.037 mmol, 1.0 equiv.) was added to a vial charged with EtOH (20.0 mL) and sonicated for 5 min, yielding mixture B. Mixture B was subsequently added to mixture A, and the reaction was allowed to proceed for 4 h at 100 °C. After the reaction finished, the as-synthesized UU-206 MOF was collected by centrifugation at 3800 rpm for 10 min. The collected MOF was further washed with DMF (three times ×20 mL each time) and EtOH (three times ×10 mL each time). The washed UU-205 MOF was finally dried under vacuum at 70 °C overnight, yielding a pale-yellow solid.

2.3. Characterization

Powder X-ray diffraction (PXRD) diffractograms were obtained on a Bruker D8 Advance diffractometer using Cu $K\alpha_{1,2}$ ($\lambda = 1.54$ Å) radiation at an operating voltage of 40 kV and a current of 40 mA. Gas sorption isotherms of CH_4, CO_2, N_2, O_2, and SF_6 were recorded on a Micromeritics ASAP 2020 instrument at either 20 °C using a circulating water bath or at −195 °C in a liquid N_2 bath. The sample was degassed at 150 °C for 5 h under dynamic vacuum prior to the measurements. Infrared spectra were collected on a Bruker Tensor 27 Fourier Transform (FTIR) spectrometer. The thermogravimetric decomposition profile of the material was recorded on a Mettler TGA/DSC 3+ at a heating rate of 10 °C min^{-1} between 30 and 800 °C in airflow (60 mL min^{-1}). Scanning electron microscopy (SEM) images were collected on a Zeiss Merlin Field Emission (FE) SEM operated at 50 pA and an acceleration voltage of 2.5 kV. Survey and high-resolution X-ray photoelectron spectroscopy (XPS) spectra were collected on a Ulvac PHI Quantera II instrument using monochromatic Al Kα (1486.6 eV) radiation, under a flow of low-energy electrons and argon ions to compensate for charge build-up. Solid-state diffuse reflectance UV-vis spectrum of the material was obtained on a PerkinElmer Lambda 900 UV/VIS(NIR spectrophotometer in the range of 250–800 nm. Electrochemical measurements were carried out on a CH Instruments CHI 660D electrochemical workstation using a three-electrode setup—Ag/AgCl as the reference electrode and a platinum wire as the counter electrode—using 0.2 M Na_2SO_4 as electrolyte. The working electrode was prepared by drop-casting a dispersion of the MOF (5 mg MOF in EtOH and 4.8 wt% polyvinylidene fluoride (PVDF)) onto a 1 cm^2 area on an indium tin oxide (ITO) electrode. Nuclear magnetic resonance (NMR) spectra (^1H, ^{13}C, and ^{19}F) were acquired on a JEOL 400 MHz spectrometer. Chemical shifts (δ) are reported in ppm relative to residual solvent signals ($CDCl_3$, $\delta_H = 7.26$ ppm, $\delta_C = 77.16$ ppm; or CD_3OD, $\delta_H = 3.31$ ppm, $\delta_C = 49.00$ ppm). The following abbreviations are used to describe peak patterns when appropriate: s (singlet), d (doublet), t (triplet), q (quartet), quint (quintet), m (multiplet), br (broad). Reactions were monitored by ^1H NMR and/or TLC on silica gel plates (60 Å porosity, 250 μm thickness). Analytical thin-layer chromatography (TLC) was performed using pre-coated aluminium-backed plates (Merck Kieselgel 60 F_{254}) and visualized using potassium permanganate stain, and/or UV light with a wavelength of 254 nm. Flash column chromatography was performed using silica gel Merck-60 (neutralized with Et_3N).

3. Results and discussions

3.1. Structure and topology of UU-206

UU-206 was solvothermally obtained by reacting $Bi(NO_3)_3 \cdot 5H_2O$ and the branched π-conjugated carboxylic linker H_8ettb (4′,4‴,4⁗,4⁗′′-(ethene-1,1,2,2-tetrayl)tetrakis((([1,1′-biphenyl]-3,5-dicarboxylic acid))) in a solution of DMF/EtOH (1 : 4 v/v) and HCOOH at 100 °C for 4 h. The framework crystalized in the monoclinic space group *P*2/*m*, with unit cell parameters of $a = 11.0903(19)$ Å, $b = 9.9420(8)$ Å, $c = 34.270(4)$ Å, and $\beta = 94.397(14)°$ (Table S1 and Fig. S1) as revealed by continuous rotation 3-dimensional electron diffraction (3D ED) (Fig. 1d). The Bi^{3+} ions coordinate to six and seven oxygen atoms from three separate ettb linkers, respectively, from which one bridging oxygen atom is shared. This coordination environment gives rise to two unique nodes, (BiO_6) and (BiO_7), with Bi–O bond lengths ranging from 2.157 to 2.708 Å, forming a dimeric (Bi_2O_{12}) cluster (Fig. 1a).

Similarities between the inorganic building unit of UU-206 and the Bi-MOF NOTT-220 can be observed, owing to the

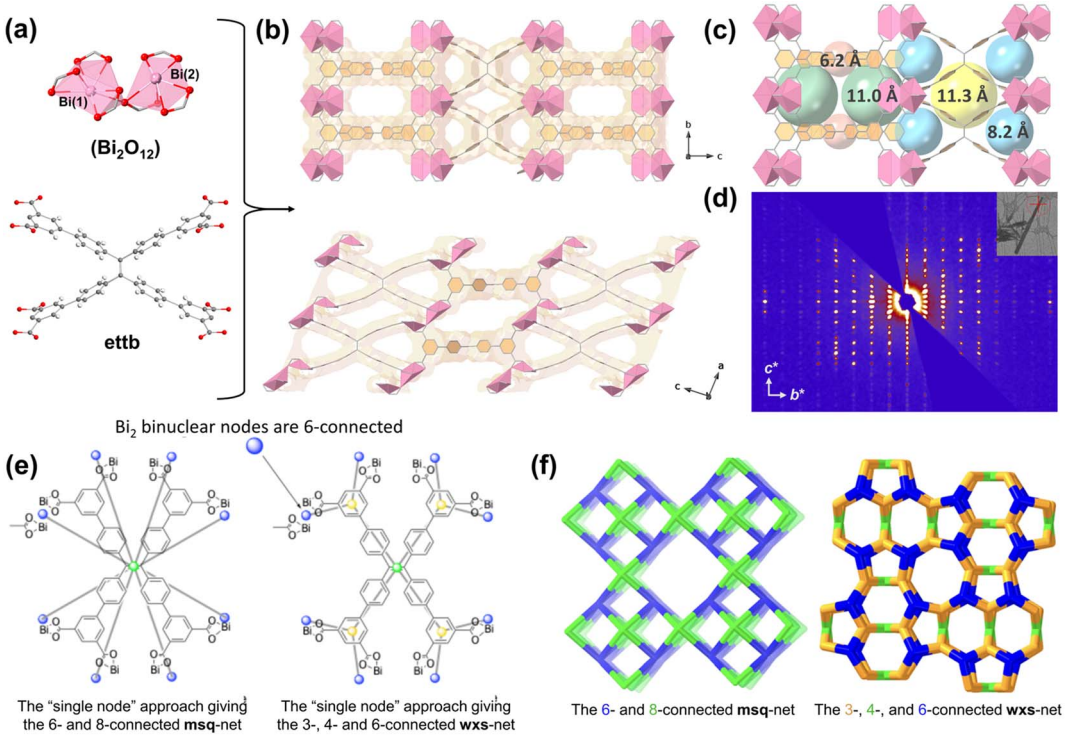

Fig. 1 (a) Conjugated molecular structure of ettb linker and (Bi_2O_{12}) cluster of UU-206. Colour code: oxygen (red), carbon (gray), and bismuth (pink). (b) Crystal structure of UU-206 as viewed along the crystallographic *a*- and *c*-axis, along with the van der Waals surface (light orange). (c) Pore cavities in the framework structure, highlighted by green, blue, yellow, and orange spheres. (d) 3D ED pattern along the [100] plane and insert of crystal. (e) Left: The "single node" deconstruction considering only the linkers' overall connectivity, giving a 6- and 8-connected net. Right: The "all node" deconstruction, considering all branch points of the linkers, yielding a 3-, 4-, and 6-connected net. (f) The ideal, most symmetric forms of **msq** and **wxs**, the two nets that can be used to describe the network in UU-206.

chemical structure of the organic linkers, specifically the spatial arrangement of neighbouring carboxylate groups.[11] The interconnection between the Bi-clusters and ettb linkers forms a continuous 3D framework structure that exhibits four unique 1D channels running along the crystallographic *a*- and *c*-axis (Fig. 1b) with pore diameters ranging from approximately 6 to 11 Å (Fig. 1c). The structure exhibits substantial disorder of the benzene rings, with one of the ettb linkers having an occupancy of 0.5, resulting in a formulation of $[(Bi_2)_4(ettb)_3]$. Identification of a proper network topology, therefore, becomes less straightforward. However, the observed linker disorder is not random. The linkers with an occupancy of 0.5 are situated at neighbouring but mutually excluding sites, as phenyl groups would otherwise collide (see Fig. S3). To derive a network topology, we assume the same sites are occupied throughout the crystal and in the most symmetric fashion. We explore the two common approaches to network topology analysis, the "all node" deconstruction, considering all branch points of the linkers, and the "single node" deconstruction, considering only the linkers' overall connectivity (Fig. 1e).[22] The latter approach is a necessary starting point for UU-206 because of the disorder, giving the **msq** net, while the "all node" deconstruction, giving the **wxs** net, has been shown to differentiate between framework isomers.[23] Details of the topological analysis are given in the SI (Section 1.2), and the two nets are displayed in Fig. 1f.

The only previous observation of these two nets was in the MOF MMPF-2 based on tetrakis(3,5-dicarboxyphenyl)porphyrin and a 6-connected distorted trigonal prism-shaped Co_3 node.[24] MMPF-2 was originally described by the "single node" deconstruction as an **msq** net.[24] O'Keeffe and co-workers later analysed MMPF-2 with the "all nodes" approach and described the 3-, 4-, and 6-connected five-nodal **wxs** net.[25] The latter one is built up by triangles, squares, and flattened trigonal prisms. The "all nodes" approach on UU-206 more closely follows the real topology, and reveals three distinct channels (Fig. 1f), one large and two small. Using just arbitrary values of edges and node sizes, the three apparent channels in the **wxs** net have radii proportions 4 : 3 : 2. It should be noted that not only are these topologies very rare, but the situation of what might be called "topology scrambling" is also unusual. The models we propose, **msq** and **wxs**, are the most symmetric arrangements consistent with the crystallography data, but most likely other configurations co-exist. This is distinctively different from the kind of defect engineering that replaces an entire linker with two capping groups like formate or acetate.

3.2. Porosity and gas sorption

The highly porous nature of UU-206 was confirmed by nitrogen (N_2) sorption at −196 °C (77 K) (Fig. 2a and b). The MOF

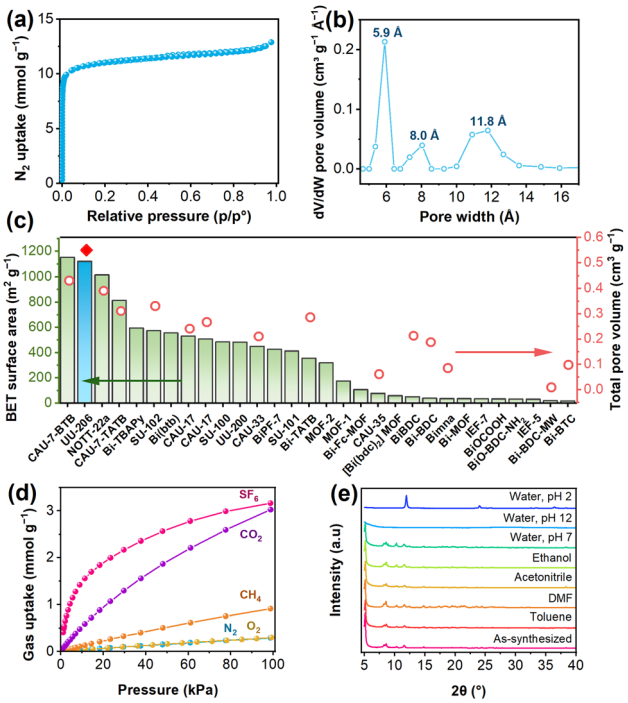

Fig. 2 (a) N_2 sorption isotherm recorded at −196 °C (or 77 K), (b) DFT pore size distribution, (c) comparison of the BET surface area and total pore volume of UU-200 and other Bi-based MOFs, (d) CH_4, CO_2, N_2, O_2, and SF_6 adsorption isotherms recorded at 20 °C, and (e) PXRD patterns of UU-206 after treatment in various solvents for 24 h.

exhibited a Brunauer–Emmett–Teller (BET) surface area and total pore volume (V_{tot}) of 1119 m^2 g^{-1} and 0.55 cm^3 g^{-1}, respectively. These values are consistent with the calculated specific surface area of 1230 m^2 g^{-1} and pore volume of 0.63 cm^3 g^{-1}, obtained in Mercury,[26] and were among the highest reported for all Bi-MOFs (Fig. 2c).[6–11,14,20,27–43] The surface area of UU-206 was only comparable to that of CAU-7-BTB (1150 m^2 g^{-1}, V_{tot} = 0.43 cm^3 g^{-1})[7] and NOTT-22a (1014 m^2 g^{-1}, V_{tot} = 0.39 cm^3 g^{-1}),[11] two of the most porous Bi-based MOFs to date, yet surpasses both of the materials in pore volume (Fig. 2c and Table S2). Furthermore, the framework of UU-206 remained stable after activation, as evident by the DFT pore size distribution (Fig. 2b) showing the presence of 5.9, 8.0, and 11.8 Å pores. The experimentally obtained pore sizes were in good agreement with the pore cavities estimated from the crystal structure obtained under high vacuum (Fig. 1c).

The high porosity of UU-206 can be utilized for gas sorption, especially for gases that have similar dimensions to the pore diameter of the framework. Gas sorption experiments at 20 °C with CO_2, O_2, N_2, CH_4, and SF_6 showed that the uptake of the potent greenhouse gas SF_6 (3.17 mmol g^{-1}) on UU-206 was the highest of all gases at 100 kPa, followed by CO_2 (3.02 mmol g^{-1}), CH_4 (0.91 mmol g^{-1}), O_2 (0.30 mmol g^{-1}), and N_2 (0.29 mmol g^{-1}) (Fig. 2d). The high uptake of SF_6 and CO_2 over O_2, N_2, and CH_4 can be attributed to both size effects and the electrostatic properties of the molecules.[44,45] The characteristic quadrupole moment of CO_2 molecules is known to give rise to attractive quadrupole-π interactions with electron-rich aromatic

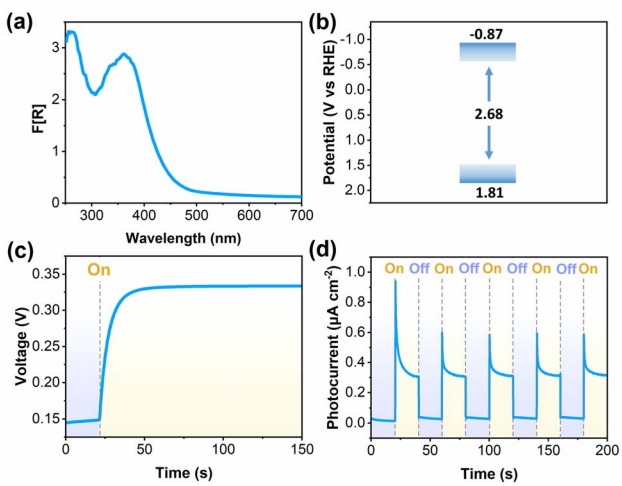

Fig. 3 (a) Solid-state diffuse reflectance UV-vis spectrum of UU-206, (b) band position diagram, (c) open circuit voltage (OCV), and (d) photocurrent response during visible light (λ > 400 nm) illumination.

moieties, leading to adsorption of the molecules onto such sites.[46] In comparison, the highly symmetric SF_6 molecules only interact with weak van der Waals (vdW) forces. However, the 5.9 and 8.0 Å diameter pores of UU-206 may have enhanced vdW interaction with SF_6 molecules (5.5 Å), when compared with CO_2 (3.3 Å), because there is increased contact between the SF_6 molecules and the pore surface, which also increases adsorbent–adsorbate interactions due to the high polarizability of the molecules and the electron-rich sites in the pores.[47] These interactions, therefore, enable UU-206 to achieve comparable or superior CO_2 and SF_6 uptake compared to other Bi-MOFs (Table S3). Water sorption on UU-206 at 20 °C (Fig. S8d) revealed that the framework exhibited weak hydrophilic properties, possessing an uptake of 8.78 mmol g^{-1} (0.16 g g^{-1}) at p/p^0 = 0.9. Furthermore, the MOF demonstrates excellent structural stability across various polar and nonpolar solvents over a 24-hour period, however, degrading in highly acidic and basic environments (Fig. 2d).

3.3. Optical and photocatalytic properties

The utilization of bismuth photocatalyst materials has, to a large extent, included bismuth oxides and binary bismuth composites, *i.e.*, bismuth titanate (*e.g.* $Bi_4Ti_3O_{12}$), bismuth tungstate (Bi_2WO_6), bismuth molybdate (Bi_2MoO_6), bismuth vanadate ($BiVO_4$), and bismuth oxyhalides (*e.g.*, BiOCl).[48,49] Assessment of UU-206 as a Bi-based photocatalyst, therefore, requires careful evaluation of the optical and electrochemical properties of the material. The optical properties of UU-206 were assessed by solid-state UV-vis spectroscopy, and the diffuse reflectance spectrum (Fig. 3a) indicate that UU-206 has an absorption range of 250 to 450 nm, showing the MOFs capability to harvest visible light. The optical band gap (E_g) of UU-206 was evaluated from the corresponding Tauc plot (Fig. S10a) to be 2.68 eV (Fig. 3b). It falls within the range of other Bi-based photocatalysts such as Bi_2O_3 (2.1–2.8 eV),[50] $BiVO_4$ (2.4 eV),[51] IEF-5 (2.4 eV),[37] and CAU-17 (3.83 eV).[52] Mott–

Table 1 Optimization and reaction scope of the photocatalytic oxidative condensation of amines to imines using UU-206[a]

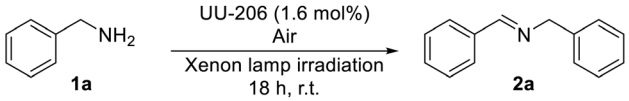

Entry	Deviation from standard conditions	Yield **2a** (%)[b]
1	None	86
2	Absence of catalyst	Trace
3	No light	n.d
4	Under N_2 atmosphere	Trace
5	Addition of TEMPO (2 equiv.)	n.d
6[c]	Using H_8ettb instead of UU-206	8
7[d]	Using $Bi(NO_3)_3 \cdot 5H_2O$ instead of UU-206	Trace
8[d]	Using Bi_2O_3 instead of UU-206	Trace
9[e]	Using CAU-7 instead of UU-206	26
10[e]	Using UU-200 instead of UU-206	Trace

[a] Conditions: **1a** (0.2 mmol), UU-206 (2.5 mg, 1.6 mol% calculated based on ettb linkers), MeCN (anhyd., 2.0 mL, 0.05 M), Xenon lamp irradiation equipped with a 400 nm UV cut-off filter. Reaction was carried out under air atmosphere at room temperature in a water-cooled jacketed beaker for 18 h. [b] Reaction yields were determined by ^{1}H NMR using toluene (0.2 mmol) as an internal standard. [c] H_8ettb (1.6 mol%) was used. [d] $Bi(NO_3)_3 \cdot 5H_2O$ (4.3 mmol%) or Bi_2O_3 (2.1 mol%) was used. [e] CAU-7 (1.6 mol% based on btb linker) or UU-200 (1.6 mol% based on btc linker) was used.

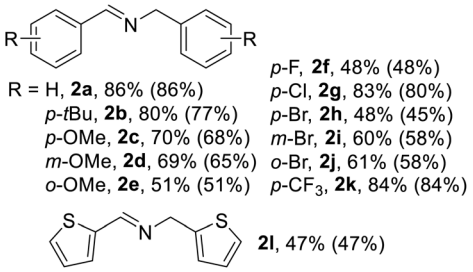

Schottky experiments (Fig. S10b) and the valence-band X-ray photoelectron spectroscopy (XPS) spectrum (Fig. S8d) of the framework were used to estimate the lowest unoccupied molecular orbital (LUMO) and highest occupied molecular orbital (HOMO) of UU-206. The flat-band potential, inferred from the Mott–Schottky plot, was determined to be −0.79 eV *vs.* Ag/AgCl at pH 7, and the valence band was 1.8 eV (Fig. S8d), which corresponds well with the estimated potential (1.89 eV) calculated from the band gap and LUMO potential. The open-circuit voltage (OCP) measured under visible light (Xenon lamp, λ > 400 nm) illumination (Fig. 3c) was *ca* 180 mV. This value was higher than that of other visible-light-active MOF photocatalysts, such as NUT-9 (7 mV)[53] and Ni-TBAPy-NB (150 mV),[54] and was found to be comparable to MOF/semiconductor composite materials, such as Ov-$BiVO_4$/MIL-101 (180 mV).[55] The photocurrent response of UU-206 (Fig. 3d) further demonstrated that the MOF exhibited a current density of *ca* 0.35 μA cm^{-2}, confirming efficient charge separation of the generated photoelectrons and holes in the material.

Visible light-driven organic transformations have attracted considerable attention as efforts have been made to develop greener and more sustainable synthetic processes. In this study, we focused on the use of UU-206 as an efficient heterogeneous photocatalyst for the oxidative condensation of amines (Table 1) to imines – an important nitrogen-containing building block in the synthesis of a wide range of biologically active compounds and industrial synthetic substrates.[56–60] Under optimized reaction conditions, consisting of benzylamine **1a** (0.2 mmol) as the model substrate, UU-206 (1.6 mol%) as the photocatalyst, in anhydrous MeCN solvent (0.05 M), Xenon light irradiation (with a 400 nm UV cut-off filter) for 16 h at room temperature, the imine desired product was formed in 86% yield (Table 1, entry 1). In the absence of the photocatalyst or light, a negligible amount of imine **2a** was obtained (Table 1, entries 2–3). The reaction was inhibited under a N_2 atmosphere or upon the addition of a TEMPO radical scavenger (Table 1, entries 4–5), confirming the involvement of oxygen radical species in photocatalytic oxidative condensation of amines. Control experiments using H_8ettb linker resulted in only 8% yield, while using $Bi(NO_3)_3 \cdot 5H_2O$ or Bi_2O_3 as catalysts only yielded trace amounts of the product (Table 1, entries 6–8). This result demonstrated the noteworthy photocatalytic performance of UU-206 itself over its structural components. In the photocatalytic oxidative condensation of amine, UU-206 is also superior to other bismuth-based MOFs tested under the same conditions (Table 1), *i.e.*, CAU-7 and UU-200, as CAU-7 gave 26% yield of **2a** while UU-200 formed only a trace amount of the imine product. Catalyst recyclability study with a shorter reaction time of 5 h compared to the standard conditions was carried out. The recycled catalyst showed a lower yield compared to the pristine

UU-206; however, similar yield was achieved after 18 h of reaction (see SI, Section 1.4 for more details).

The scope of the photocatalytic oxidative amine condensation was explored under the optimized conditions. Good to excellent yields of substituted (*E*)-*N*-benzyl-1-phenylmethanimines **2a–k** were obtained from benzylamine derivatives **1a–k**. Furthermore, thiophene heterocyclic imine **2l** was also achieved in 47% under optimized conditions. We envision that under photo-irradiation, energy harvested by the photosensitizing ettb linkers accounts for electron–hole generation,[61] and the Bi-MOF's intrinsic built-in electric fields (BIEFs) play a primary role in charge separation.[62] The photogenerated electrons are then transferred to the Bi-oxo clusters *via* linker-to-metal charge transfer (LMCT).[63–65] The combination of photosensitizing ettb linkers and Bi-oxo clusters, therefore, exhibits a synergic effect in the photocatalytic condensation of amines. Based on literature review,[66–69] we can at this stage propose that under light irradiation, holes and electrons are generated in UU-206. Photogenerated electrons are transferred to O_2 to form superoxide radical anions ($O_2^{\bullet-}$),[70] and holes react with amines to form benzylamine radical cations. The subsequent reaction between $O_2^{\bullet-}$ and the benzylamine radical cation gives rise to benzylimine, which readily undergoes hydrolysis to yield benzaldehyde. Consequently, benzaldehyde can thereafter react with benzylamine **1a** to form the imine homo-coupling product **2a** (Fig. 4).

As a proof-of-concept experiment, we perform the photocatalytic amine condensation in a more sustainable fashion by replacing the Xenon lamp with low-intensity natural sunlight at high latitude (~59.9° N) in early spring. The reaction, which was set up outdoors on a day with light cloud coverage at a recorded daytime temperature of 7 °C, was also shortened from 18 h (using Xenon lamp) to only 5 h (using natural sunlight). Under these conditions, an increased loading of the UU-206 catalyst of 6.4 mol% was employed. Imine **2a** was formed in a synthetically useful yield of 25% using natural sunlight as the light source, atmospheric air as the oxidant, and at ambient temperature within 5 h. The reduced yield of product **2a**, as compared to the optimized conditions, can be attributed to the limited availability of intense, direct sunlight. This limitation can be addressed using various strategies, for instance, through modifications of the framework structure of the MOF by incorporating visible-light-active chromophoric moieties into the organic linker to enhance light harvesting, as well as introducing defects or heterojunctions to suppress charge recombination and promote the formation of long-lived excited states.[71–75] However, overall, this experiment demonstrates that UU-206 can be an efficient heterogeneous photocatalyst in aerobic oxidative condensation of amines to imines. This finding also emphasizes the sustainable aspect of our approach towards greener chemical production.

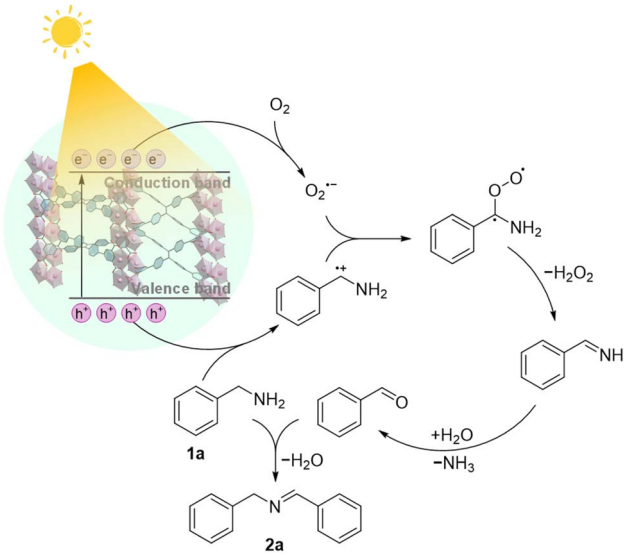

Fig. 4 Proposed mechanism of the photocatalytic condensation of amines on UU-206.

4. Conclusions

We have developed Bi-MOF UU-206 by combining a photosensitising octatopic tetraphenylethylene-based linker with binuclear (Bi_2O_{12}) clusters to form a highly porous three-dimensional framework that can be described by the rare **wxs** net and an unusual topology scrambling. UU-206 exhibits one of the highest porosities reported for Bi-MOFs to date, together with well-defined channels that enable high uptake of greenhouse gases, particularly SF_6 and CO_2, and good selectivity over N_2, CH_4, and O_2. The framework is structurally robust, retaining its crystallinity after activation, gas sorption, and exposure to a range of solvents. Optical and electrochemical studies reveal that UU-206 is a visible light-absorbing semiconductor with efficient charge separation arising from the combination of the macroconjugated chromophore linker and the Bi-containing inorganic nodes. These features translate into excellent photocatalytic performance in the aerobic oxidative condensation of amines to imines under mild conditions, where UU-206 clearly outperforms its individual components and related Bi-based MOFs, although, naturally, a full-scale mechanistic investigation of the MOF as a photocatalyst would be an essential next step to correctly assess the application potential of the MOF as a photocatalyst. Importantly, the reaction can be driven by low-intensity natural sunlight under cold, high-latitude conditions, highlighting the potential of UU-206 as a platform for solar-driven green chemical transformations. More broadly, this work illustrates how integrating polytopic chromophore linkers with Bi cluster nodes can be used as a design strategy to access multifunctional MOFs that combine high porosity, rare topology, and efficient visible light photocatalysis.

Conflicts of interest

There are no conflicts to declare.

Data availability

CCDC 2489753 contains the supplementary crystallographic data for this paper.[76]

The data supporting this article have been included as part of the supplementary information (SI). Supplementary information: experimental details for 3D ED collection, topological analysis, and photocatalytic condensation of amines, as well as Fig. S1–S36 and Tables S1–S3. See DOI: https://doi.org/10.1039/d6ta01278g.

Acknowledgements

The authors acknowledge support from the Wallenberg Foundation (KAW2023.0213), Swedish Research Council (Grant No. 2020-04029, 2022-02939, and 2024-04068), Olle Engkvists Foundation, and the Swedish Foundation for Strategic Environmental Research (Mistra) (Project Name: Mistra TerraClean, Project number 2015/31). K. S. P. thanks the Carlsberg Foundation for a Carlsberg Foundation Young Researcher Fellowship (CF21-0416).

References

1 H. Furukawa, K. E. Cordova, M. O'Keeffe and O. M. Yaghi, *Science*, 2013, **341**, 1230444.
2 S. Kitagawa, R. Kitaura and S. Noro, *Angew. Chem., Int. Ed.*, 2004, **43**, 2334–2375.
3 L. Jiao, J. Y. R. Seow, W. S. Skinner, Z. U. Wang and H.-L. Jiang, *Mater. Today*, 2019, **27**, 43–68.
4 X. Zhang, A. Chen, M. Zhong, Z. Zhang, X. Zhang, Z. Zhou and X.-H. Bu, *Electrochem. Energy Rev.*, 2019, **2**, 29–104.
5 A. K. Inge, M. Köppen, J. Su, M. Feyand, H. Xu, X. Zou, M. O'Keeffe and N. Stock, *J. Am. Chem. Soc.*, 2016, **138**, 1970–1976.
6 M. Köppen, O. Beyer, S. Wuttke, U. Lüning and N. Stock, *Dalton Trans.*, 2017, **46**, 8658–8663.
7 M. Feyand, E. Mugnaioli, F. Vermoortele, B. Bueken, J. M. Dieterich, T. Reimer, U. Kolb, D. de Vos and N. Stock, *Angew. Chem., Int. Ed.*, 2012, **51**, 10373–10376.
8 E. S. Grape, H. Xu, O. Cheung, M. Calmels, J. Zhao, C. Dejoie, D. M. Proserpio, X. Zou and A. K. Inge, *Cryst. Growth Des.*, 2020, **20**, 320–329.
9 E. S. Grape, J. G. Flores, T. Hidalgo, E. Martínez-Ahumada, A. Gutiérrez-Alejandre, A. Hautier, D. R. Williams, M. O'Keeffe, L. Öhrström, T. Willhammar, P. Horcajada, I. A. Ibarra and A. K. Inge, *J. Am. Chem. Soc.*, 2020, **142**, 16795–16804.
10 M. Åhlén, E. Kapaca, D. Hedbom, T. Willhammar, M. Strømme and O. Cheung, *Microporous Mesoporous Mater.*, 2022, **329**, 111548.
11 M. Savage, S. Yang, M. Suyetin, E. Bichoutskaia, W. Lewis, A. J. Blake, S. A. Barnett and M. Schröder, *Chem. –Eur. J.*, 2014, **20**, 8024–8029.
12 Y. Wang, H. Sun, Z. Yang, Y. Zhu and Y. Xia, *Carbon Neutralization*, 2024, **3**, 737–767.
13 I. Mondal, D. Ghosh, U. Pal and S. Mistry, *ChemCatChem*, 2025, **17**, e202500022.
14 G. Wang, Q. Sun, Y. Liu, B. Huang, Y. Dai, X. Zhang and X. Qin, *Chem. –Eur. J.*, 2015, **21**, 2364–2367.
15 W. Zou, Q. Li, Q. Wu, Z. Zhang and Y. Zhou, *Chem. Eng. J.*, 2025, **505**, 159428.
16 Y. Yang, S. Peng, S. Chen, F. Kang, J. Fan, H. Zhang, X. Yu, J. Li and Q. Zhang, *Nanoscale Horiz.*, 2024, **9**, 2198–2233.
17 Y. Zhang, J. Pang, J. Li, X. Yang, M. Feng, P. Cai and H.-C. Zhou, *Chem. Sci.*, 2019, **10**, 8455–8460.
18 J.-J. Shao, J.-L. Ni, Y. Liang, X.-D. Xu and F.-M. Wang, *J. Mol. Struct.*, 2021, **1244**, 130975.
19 F.-D. Wang, K.-K. Niu, X.-Y. Yao, S. Yu, H. Liu, L.-B. Xing and P.-Z. Li, *J. Mater. Chem. A*, 2024, **12**, 16190–16199.
20 M. Köppen, A. Dhakshinamoorthy, A. K. Inge, O. Cheung, J. Ångström, P. Mayer and N. Stock, *Eur. J. Inorg. Chem.*, 2018, **2018**, 3496–3503.
21 G. Agbeworvi, A. Pakhira, S. Hariyani, W. Zaheer, A. Giem, J. R. Ayala, J. D. Ponis, S. Perez-Beltran, C. Jaye, C. Weiland, D. A. Fischer, H. S. Bazzi, M. Al-Hashimi and S. Banerjee, *Chem. Sci.*, 2025, **16**, 5129–5141.
22 C. Bonneau, M. O'Keeffe, D. M. Proserpio, V. A. Blatov, S. R. Batten, S. A. Bourne, M. S. Lah, J.-G. Eon, S. T. Hyde, S. B. Wiggin and L. Öhrström, *Cryst. Growth Des.*, 2018, **18**, 3411–3418.
23 H. Li, F. M. Amombo Noa, M. Åhlén, Z. Cao, J. Andréasson, O. Cheung and L. Öhrström, *Chem. Commun.*, 2025, **61**, 14129–14132.
24 X.-S. Wang, M. Chrzanowski, C. Kim, W.-Y. Gao, L. Wojtas, Y.-S. Chen, X. Peter Zhang and S. Ma, *Chem. Commun.*, 2012, **48**, 7173.
25 M. Li, D. Li, M. O'Keeffe and O. M. Yaghi, *Chem. Rev.*, 2014, **114**, 1343–1370.
26 C. F. Macrae, I. J. Bruno, J. A. Chisholm, P. R. Edgington, P. McCabe, E. Pidcock, L. Rodriguez-Monge, R. Taylor, J. Van De Streek and P. A. Wood, *J. Appl. Crystallogr.*, 2008, **41**, 466–470.
27 A. Thirumurugan and A. K. Cheetham, *Eur. J. Inorg. Chem.*, 2010, **2010**, 3823–3828.
28 B. Zhang, H. Xu, M. Wang, L. Su, S. Zhang, Y. Zhang and Q. Wang, *J. Environ. Chem. Eng.*, 2022, **10**, 108469.
29 S. Iram, M. Imran, F. Kanwal, S. Latif and Z. Iqbal, *Mater. Sci.*, 2020, **38**, 132–137.
30 Q.-Y. Yang, C.-Q. Wan, Y.-X. Wang, X.-F. Shen and Y.-H. Pang, *J. Hazard. Mater.*, 2023, **451**, 131148.
31 D. Wei, H. Dong, B. Ouyang, P. Chen, T. Zhang, Y. He, L. Huang and H. Wang, *Chem. Eng. J.*, 2025, **513**, 162947.
32 Y. Xiao, X. Guo, J. Liu, L. Liu, F. Zhang and C. Li, *Chin. J. Catal.*, 2019, **40**, 1339–1344.
33 V. A. Tran, T. T. Sang, N. A. Thu, V. Vo, V. T. Le, V. D. Doan, T.-T. Thi Vo and N. D. Dat, *RSC Adv.*, 2024, **14**, 31171–31182.
34 Z. Zhang, S. B. Peh, C. Kang, K. Yu and D. Zhao, *Angew. Chem., Int. Ed.*, 2022, **61**, e202211808.
35 V. H. Nguyen, A. L. H. Pham, V.-H. Nguyen, T. Lee and T. D. Nguyen, *Chem. Eng. Res. Des.*, 2022, **177**, 321–330.
36 E. P. Gómez-Oliveira, D. Reinares-Fisac, L. M. Aguirre-Díaz, F. Esteban-Betegón, M. Pintado-Sierra, E. Gutiérrez-Puebla,

M. Iglesias, M. Ángeles Monge and F. Gándara, *Angew. Chem., Int. Ed.*, 2022, **61**, e202209335.
37 A. García-Sánchez, M. Gomez-Mendoza, M. Barawi, I. J. Villar-Garcia, M. Liras, F. Gándara and V. A. De La Peña O'Shea, *J. Am. Chem. Soc.*, 2020, **142**, 318–326.
38 P. Salcedo-Abraira, C. Biglione, S. M. F. Vilela, E. Svensson Grape, N. Ureña, F. Salles, M. T. Pérez-Prior, T. Willhammar, P. Trens, A. Várez, A. K. Inge and P. Horcajada, *Chem. Mater.*, 2023, **35**, 4329–4337.
39 V. H. Nguyen, T. D. Nguyen and T. Van Nguyen, *Top. Catal.*, 2020, **63**, 1109–1120.
40 E. Svensson Grape, A. J. Chacón-García, S. Rojas, Y. Pérez, A. Jaworski, M. Nero, M. Åhlén, E. Martínez-Ahumada, A. E. Galetsa Feindt, M. Pepillo, M. Narongin-Fujikawa, I. A. Ibarra, O. Cheung, C. Baresel, T. Willhammar, P. Horcajada and A. K. Inge, *Nat. Water*, 2023, **1**, 433–442.
41 P. Lamagni, M. Miola, J. Catalano, M. S. Hvid, M. A. H. Mamakhel, M. Christensen, M. R. Madsen, H. S. Jeppesen, X. Hu, K. Daasbjerg, T. Skrydstrup and N. Lock, *Adv. Funct. Mater.*, 2020, **30**, 1910408.
42 H. Ouyang, N. Chen, G. Chang, X. Zhao, Y. Sun, S. Chen, H. Zhang and D. Yang, *Angew. Chem., Int. Ed.*, 2018, **57**, 13197–13201.
43 M. Köppen, V. Meyer, J. Ångström, A. K. Inge and N. Stock, *Cryst. Growth Des.*, 2018, **18**, 4060–4067.
44 A. D. Buckingham and R. L. Disch, *Proc. R. Soc. London, A*, 1063, **273**, 275–289.
45 P. W. Fowler, H. M. Kelly and E. Steiner, *Chem. Phys. Lett.*, 1993, **203**, 189–194.
46 A. Torrisi, C. Mellot-Draznieks and R. G. Bell, *J. Chem. Phys.*, 2009, **130**, 194703.
47 M.-B. Kim, K.-M. Kim, T.-H. Kim, T.-U. Yoon, E.-J. Kim, J.-H. Kim and Y.-S. Bae, *Chem. Eng. J.*, 2018, **339**, 223–229.
48 L. Zhang, Y. Li, Q. Li, J. Fan, S. A. C. Carabineiro and K. Lv, *Chem. Eng. J.*, 2021, **419**, 129484.
49 L. Chen, B. Guan, J. Guo, Y. Chen, Z. Ma, J. Chen, S. Yao, C. Zhu, H. Dang, K. Shu, Z. Guo, C. Yi, K. Shi, Y. Li, J. Hu and Z. Huang, *Catal. Sci. Technol.*, 2023, **13**, 5478–5529.
50 H.-Y. Jiang, J. Liu, K. Cheng, W. Sun and J. Lin, *J. Phys. Chem. C*, 2013, **117**, 20029–20036.
51 C. Xiao, S. Assavachin, W. Hahn, L. Wang, K. Van Benthem and F. E. Osterloh, *J. Mater. Chem. A*, 2025, **13**, 7834–7844.
52 S. Dong, L. Wang, W. Lou, Y. Shi, Z. Cao, Y. Zhang and J. Sun, *Ultrason. Sonochem.*, 2022, **91**, 106223.
53 J. Gao, J. Miao, P.-Z. Li, W. Y. Teng, L. Yang, Y. Zhao, B. Liu and Q. Zhang, *Chem. Commun.*, 2014, **50**, 3786–3788.
54 L. Liu, S. Du, X. Guo, Y. Xiao, Z. Yin, N. Yang, Y. Bao, X. Zhu, S. Jin, Z. Feng and F. Zhang, *J. Am. Chem. Soc.*, 2022, **144**, 2747–2754.
55 Y. Xin, J. Tian, X. Xiong, C. Wu, S. A. C. Carabineiro, X. Yang, Z. Chen, Y. Xia and Y. Jin, *Adv. Mater.*, 2025, **37**, 2417589.
56 C. M. Da Silva, D. L. Da Silva, L. V. Modolo, R. B. Alves, M. A. De Resende, C. V. B. Martins and Â. De Fátima, *J. Adv. Res.*, 2011, **2**, 1–8.
57 N. T. Patil and Y. Yamamoto, *Chem. Rev.*, 2008, **108**, 3395–3442.
58 R. W. Layer, *Chem. Rev.*, 1963, **63**, 489–510.
59 R. D. Patil and S. Adimurthy, *Asian J. Org. Chem.*, 2013, **2**, 726–744.
60 M. E. Belowich and J. F. Stoddart, *Chem. Soc. Rev.*, 2012, **41**, 2003.
61 C. Mu, L. Zhang, G. Li, Y. Hou, H. Liu, Z. Zhang, R. Zhang, T. Gao, Y. Qian, C. Guo, G. He and M. Zhang, *Angew. Chem., Int. Ed.*, 2023, **62**, e202311137.
62 Y. Peng, Y. Liu, H. Wang, Y. Hao, S. Wang, J. Luo and B. Zou, *ACS Appl. Mater. Interfaces*, 2025, **17**, 43101–43111.
63 I. Mondal, D. Ghosh, U. Pal and S. Mistry, *ChemCatChem*, 2025, **17**, e202500022.
64 M. Ingham, A. Aziz, D. Di Tommaso and R. Crespo-Otero, *Mater. Adv.*, 2023, **4**, 5388–5419.
65 R. Haldar, A. Ghosh and T. K. Maji, *Chem. Commun.*, 2023, **59**, 1569–1588.
66 C. Xu, H. Liu, D. Li, J.-H. Su and H.-L. Jiang, *Chem. Sci.*, 2018, **9**, 3152–3158.
67 Y. Zhi, K. Li, H. Xia, M. Xue, Y. Mu and X. Liu, *J. Mater. Chem. A*, 2017, **5**, 8697–8704.
68 Y. Liu, K. Ji, J. Wang, H. Li, X. Zhu, P. Ma, J. Niu and J. Wang, *ACS Appl. Mater. Interfaces*, 2022, **14**, 27882–27890.
69 Q. Fan, L. Zhu, X. Li, H. Ren, H. Zhu, G. Wu and J. Ding, *New J. Chem.*, 2021, **45**, 13317–13322.
70 M. Hayyan, M. A. Hashim and I. M. AlNashef, *Chem. Rev.*, 2016, **116**, 3029–3085.
71 X. Huang, Z. Wang, Y. Zhong, Y. Jiang, S. Chen, J. Chen, S. Deng and J. Wang, *Chem. Eng. J.*, 2025, **507**, 160812.
72 Y. Rong, X. Pan, X. Wang, S. Zheng, Z. Xin, S.-B. Wang and Z. Wang, *Nanoscale*, 2026, DOI: 10.1039/D6NR00401F.
73 C. Zhang, C. Xie, Y. Gao, X. Tao, C. Ding, F. Fan and H. Jiang, *Angew. Chem.*, 2022, **134**, e202204108.
74 Z. Guo, X. Liu, Y. Che and H. Xing, *Inorg. Chem.*, 2024, **63**, 13005–13013.
75 Z. Huang, Y. Wang, M. Qi, M. Conte, Z. Tang and Y. Xu, *Angew. Chem.*, 2024, **136**, e202412707.
76 CCDC 2489753: Experimental Crystal Structure Determination, 2026, DOI: 10.5517/ccdc.csd.cc2pksmp.

